

A three-dimensional study of the hole-tone feedback problem

Mikael A. Langthjem† and Masami Nakano‡

†*Graduate School of Science and Engineering, Yamagata University,
Jonan 4-3-16, Yonezawa, Yamagata 992-8510, Japan*

‡*Institute of Fluid Science, Tohoku University,
Katahira 2-1-1, Aoba-ku, Sendai, Miyagi 980-8577, Japan*

Abstract

A method for simulating the hole-tone feedback cycle (Rayleigh's bird-call), based on a three-dimensional discrete vortex method, is described. Evaluation of the sound generated by the self-sustained flow oscillations is based on the Powell-Howe theory of vortex sound and a boundary integral/element method. While the basic problem is inherently axisymmetric, the purpose of developing a full three-dimensional model is to investigate the influence of non-axisymmetric perturbations of the jet on the sound generation. Experimentally, such perturbations can be applied at the jet nozzle via piezoelectric or electro-mechanical actuators, placed circumferentially inside the nozzle at its exit. In the mathematical/numerical model, this is simulated by wave motions of a deformable nozzle. Both standing and traveling (rotating) waves are considered. It is shown that a considerable reduction of the sound generation is possible.

1 Introduction

Self-sustained fluid oscillations can occur in a variety of practical applications where a shear layer impinges upon a solid structure [19, 24, 25]. The present paper is concerned with such oscillations in the hole-tone problem [3, 22], where a fluid jet issuing from a circular hole in a plate (or from a nozzle) impinges upon a (second) plate with a similar hole, located a little downstream from the nozzle. Self-sustained oscillations of the jet are generated, accompanied by sound with a definite tone. The common teakettle whistle and the bird-call are examples of utilization of this phenomenon. The principle of the system is illustrated by Fig. 1.

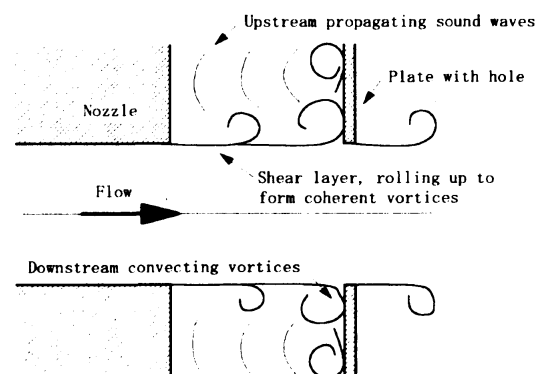


Figure 1: Principle of the hole-tone feedback problem.

The tone generation is related to periodic roll-up of the unstable, cylindrical shear layer into big, coherent¹ ‘smoke rings’. This periodic roll-up is maintained by a feedback mechanism. In his *Theory of Sound* [22] Rayleigh explained it as follows: “When a symmetrical excrescence (‘smoke ring’) reaches the second plate, it is unable to pass the hole with freedom, and the disturbance is thrown back, probably with the velocity of sound, to the first plate, where it gives rise to a further disturbance, to grow in its turn during the progress of the jet.” In terms of this picture, the system is thus one where the sound generation is caused by synchronization [20] between the sound-generating flow and the acoustic field.

The fundamental frequency f_0 satisfies the criterion

$$\ell/u_c + \ell/c_0 = n/f_0, \quad (1)$$

where ℓ is the length of the gap between the nozzle exit and the end plate, u_c is the vortex convection velocity ($u_c/u_0 \approx 0.5 \sim 0.6$, where u_0 is the mean flow velocity), c_0 is the speed of sound, and n is a mode number which may take the values $\frac{1}{2}, 1, \frac{3}{2}, \dots$ [18]. Geometrically, n specifies the number of vortices convected from the nozzle to the end plate during each period $\tau_0 = 1/f_0$. A change in the value of n implies a corresponding ‘jump’ in the frequency f_0 when the left hand side is kept constant. This does indeed occur [3, 18]. The mechanism behind it remains unexplained.

Early, ‘qualitative’ experiments on the hole tone problem were conducted by Sondhauss and by Rayleigh [22]. More thorough and quantitative experimental studies have been carried out by Chanaud and Powell [3], Nakano et al. [18], and Meganathan and Vakili [17].

Theoretical/numerical studies are very few. It appears that focus has been on the related edge-tone problem [8]. The present authors have previously analyzed the hole-tone problem in terms of an axisymmetric formulation [14, 15]. This is appropriate and sufficient since experiments have verified that the disturbances remain axisymmetric [3]. The present work deals with a full three-dimensional model. The main purpose of developing such a model is to investigate the effects of non-axisymmetric flow disturbances, to be imposed ‘mechanically’ in experiments via piezoelectric actuators placed around the circumference inside the nozzle. Such a system has been applied to free jets by Kasagi [11]. In the numerical computations, the actuator system is simulated via a deformable nozzle.

Section 2 deals with the three-dimensional vortex method. Such methods have been reviewed by Leonard [16], and Cottet and Koumoutsakos [4], among other. Three-dimensional panel methods, for representation of solid surfaces, have been reviewed by Katz and Plotkin [12].

The acoustic analysis is the subject of Section 3. It is based on the theory of vortex sound, developed by Powell [21] and Howe [7]. The scattering by the end plate is evaluated via the use of a thin-plate (zero-thickness) boundary integral/boundary element method, developed by Terai [13, 27].

The numerical examples are presented in Section 4. Examples with perturbations show that it is possible to significantly reduce the hole-tone sound generation. Both standing and rotating wave perturbations are considered, and the latter type are found to be particularly effective. A geometrically based explanation of the sound reduction mechanism is suggested.

The paper ends, in Section 5, with a few concluding remarks.

2 The discrete vortex flow model

2.1 Vortex filament model of the jet flow

The shear layer of the jet issuing from the nozzle is represented by discrete vortex rings. These rings will be disturbed mechanically at the nozzle exit such that they lose their natural axisymmetric form, and are thus represented by three-dimensional vortex filaments. The induced

¹A thorough discussion of the meaning of ‘coherent structures in flows’ can be found in [6].

velocity $\mathbf{u}_{fv} = (u_1, u_2, u_3)_{fv}$, at position $\mathbf{x} = (x_1, x_2, x_3)$ and time t , from N_{fv} free vortex rings (fv) represented by the space curves $\mathbf{r}_j(\xi, t)$, is obtained from the generalized Biot-Savart law [16]

$$\mathbf{u}_{fv}(\mathbf{x}, t) = - \sum_{j=1}^{N_{fv}} \frac{\Gamma_j}{4\pi} \oint_{C_j(\xi)} \frac{\{\mathbf{x} - \mathbf{r}_j(\xi, t)\} \times \partial \mathbf{r}_j / \partial \xi q(|\mathbf{x} - \mathbf{r}_j(\xi, t)| / \sigma_j)}{|\mathbf{x} - \mathbf{r}_j(\xi, t)|^3} d\xi. \quad (2)$$

Here Γ_j is the strength (circulation) of the j 'th vortex ring and $C_j(\xi)$ its contour, specified as a function of the parameter ξ . The 'smoothing function' $q(y)$ represents the structure of the vortex core, with $\sigma_j(\xi, t)$ being the core radius. It eliminates the logarithmic singularity at $\mathbf{x} = \mathbf{r}_j$, and smoothes out the vorticity distribution. In the present work the Rosenhead-Moore function

$$q(\kappa) = \frac{\kappa^3}{(\kappa^2 + \alpha)^{\frac{3}{2}}} \quad (3)$$

is chosen [16]. If (2) and (3) are to give the same single-ring speed as the Gaussian core distribution

$$\varpi(\varrho) = \pi^{-\frac{3}{2}} \exp(-\varrho^2), \quad (4)$$

with the corresponding smoothing function

$$q(\kappa) = 4\pi \int_0^\kappa \varpi(\varrho) \varrho^2 d\varrho, \quad (5)$$

then the parameter α should have the value 0.413 [1]. This value is accordingly used in the numerical simulations.

The solid surfaces are represented by rectilinear vortex ring panels, made up of four straight vortex filaments, as indicated in Fig. 2. The velocity induced from such a vortex panel can be obtained by evaluating the integral in (2), with $q \equiv 1$, along the line segments between points \mathbf{y}_j and \mathbf{y}_{j+1} , $j = 1, \dots, 4$, where $\mathbf{y}_5 := \mathbf{y}_1$. The expression for the induced velocity are, e.g., given in Katz and Plotkin [12].

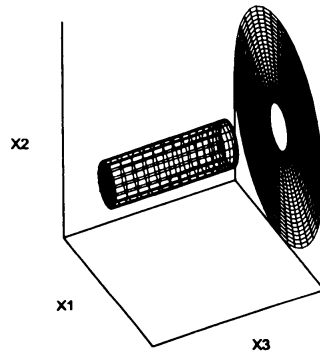


Figure 2: Solid surfaces represented by vortex panels.

The rate of continuous shedding of circulation γ from the nozzle edge is determined by using the Kutta condition, which demands that the pressure a little above the nozzle edge equals the pressure a little below [4].

The positions of the marker points on the shed vortex rings are updated by using the second-order Runge-Kutta method. The integrations over $C_j(\xi)$ in (2) are carried out using Gaussian quadrature. It should be remarked that, following an advice of Leonard [16], the core radius σ_j in (2) is replaced by $\frac{1}{2} (\sigma_m^2 + \sigma_j^2)^{1/2}$; this symmetric form will preserve linear and angular momentum.

The vortex method described above is inviscid, except for the viscous effect simulated by the Kutta condition. The vortex rings thus keep their strengths throughout the simulation, once

released. The volume of each individual ring must then be kept constant; this constraint is imposed via the equations

$$\frac{d}{dt}(\sigma_n^2 s_n)_m = 0, \quad (6)$$

where s_n is the instantaneous length of the n 'th filament. During initial numerical trial runs it was however found that vortex rings tend to 'jam up' in front of the end plate, circulating around there in a small path, disturbing the rings that are released later. In reality, such 'standing smoke rings' will be diffused away, due to viscous dissipation. To simulate this effect in a simple way, the strength of every vortex ring is reduced according to the law

$$\Gamma_j(t) = \Gamma_{j0} \left\{ 1 - \exp\left(-\frac{a^2 Re}{4u_0 t_\Gamma / r_0}\right) \right\}. \quad (7)$$

Here Γ_{j0} is the initial strength, $Re = u_0 r_0 / \nu$ is the Reynolds number with ν being the kinematic viscosity, and $t_\Gamma = t - t_{\text{release}}$ is the age of the vortex. Finally, a is a constant which is determined (by numerical experimentation) such that the decay is insignificant (negligibly small) during the time when a vortex ring moves between the nozzle exit and the end plate. [That is, a is adjusted such that the strength of a vortex ring starts to decay significantly only after it has hit the end plate, or has moved through the hole therein.]

If $a = r/r_0$, then (7) is the exact decay law for a single axisymmetric vortex ring at small Reynolds numbers, described in terms of cylindrical coordinates (x, r, ϕ) ; this was shown recently by Fukumoto and Kaplanski [5].

Rivoalen and Huberson [23] analyzed axisymmetric viscous flows via a discrete vortex method. If $a = r_i/r_0$, with r_i being the radius of the i th vortex ring, then (7) corresponds to the 'first order term' in their expression for the vortex ring strength.

It is interesting to note that (7) also is the decay law for the Lamb-Oseen vortex, which is the exact solution to the two-dimensional Navier-Stokes equations for a single line vortex in an unbounded domain, specified in terms of the polar coordinate system (r, θ) [26].

Kambe and Minota [10] derived a decay law from another two-dimensional flow, that of two superimposed shear flows, and applied it in a study of head-on collision of two axisymmetric vortex rings. The decay law obtained in this way takes the form of the error function.

3 Aeroacoustic model

3.1 The equation of vortex sound and its formal solution in terms of integral equations

To evaluate the sound generated by the self-sustained flow oscillations, the start point is taken in Howe's equation for vortex sound at low Mach numbers [8, 9]. Here the sound pressure $p(\mathbf{x}, t)$ is related to the vortex force (Lamb vector) $\mathbf{L}(\mathbf{x}, t) = \boldsymbol{\omega}(\mathbf{x}, t) \times \mathbf{u}(\mathbf{x}, t)$ via the non-homogeneous wave equation

$$\left(\frac{1}{c_0^2} \frac{\partial^2}{\partial t^2} - \nabla^2 \right) p = \rho \nabla \cdot \mathbf{L}, \quad (8)$$

where the vorticity $\boldsymbol{\omega} = \nabla \times \mathbf{u}$. The boundary conditions are

$$\frac{\partial p}{\partial \mathbf{n}} = \nabla p \cdot \mathbf{n} = 0 \text{ on the end plate, } p \rightarrow 0 \text{ for } |\mathbf{x}| \rightarrow \infty, \quad (9)$$

where \mathbf{n} denotes the outward normal vector.

Equations (8) and (9) can be reformulated into an integral equation, on the form

$$p(\mathbf{x}, t) = p_{\text{vtx}}(\mathbf{x}, t) + \sum_e \iint \frac{1}{4\pi r_{x\beta}} \left(\frac{1}{r_{x\beta}} [\tilde{p}_{\beta e}]_{t_*} + \frac{1}{c_0} \left[\frac{\partial \tilde{p}_{\beta e}}{\partial t} \right]_{t_*} \right) \cos(\mathbf{r}_{x\beta}, \mathbf{n}_\beta) d^2 \mathbf{y}_{\beta e}, \quad (10)$$

where \tilde{p}_β is the pressure difference across the end plate, and

$$p_{\text{vtx}}(\mathbf{x}, t) = - \iiint \frac{\rho}{4\pi r} \left(\frac{1}{r} [L_j]_{t_*} + \frac{1}{c_0} \left[\frac{\partial L_j}{\partial t} \right]_{t_*} \right) \frac{x_j - y_j}{r} d^3 \mathbf{y}. \quad (11)$$

In these expressions, an index t_* refers to evaluation at the retarded time $t_* = t - r/c_0$.

The pressure difference \tilde{p}_β can be evaluated by making use of the first of the equations (9), as this, by evaluating the normal derivative on the plate surface, makes the left hand side equal to zero [13, 27]. For $\mathbf{x}_\alpha \neq \mathbf{y}_\beta$, we obtain

$$\frac{\partial p_{\text{vtx}}(\mathbf{x}_\alpha, t)}{\partial n_\alpha} + \sum_e \iint \frac{1}{4\pi r_{\alpha\beta}^2} \left(\frac{1}{r_{\alpha\beta}} [\tilde{p}_{\beta e}]_{t_*} + \frac{1}{c_0} \left[\frac{\partial \tilde{p}_{\beta e}}{\partial t} \right]_{t_*} \right) d^2 \mathbf{y}_{\beta e} = 0, \quad (12)$$

while for $\mathbf{x}_\alpha = \mathbf{y}_\beta$, we obtain

$$\frac{\partial p_{\text{vtx}}(\mathbf{x}_\alpha, t)}{\partial n_\alpha} + \sum_e \left([\tilde{p}_{\beta e}]_{t_*} \int_0^{2\pi} \frac{d\theta}{4\pi R(\theta)} + \frac{1}{2c_0} \left[\frac{\partial \tilde{p}_{\beta e}}{\partial t} \right]_{t_*} \right) = 0. \quad (13)$$

In both cases, the first term is

$$\begin{aligned} \frac{\partial p_{\text{vtx}}(\mathbf{x}_\alpha, t)}{\partial n_\alpha} &= \iiint \frac{n_i}{4\pi} \left[- \left\{ \frac{\delta_{ij}}{r^3} - \frac{3}{r^5} (x_i - y_i)(x_j - y_j) \right\} [L_j]_{t_*} \right. \\ &+ \left. \left\{ \frac{\delta_{ij}}{c_0 r^2} - \frac{3}{c_0 r^4} (x_i - y_i)(x_j - y_j) \right\} \left[\frac{\partial L_j}{\partial t} \right]_{t_*} + \frac{1}{c_0^2 r^3} (x_i - y_i)(x_j - y_j) \left[\frac{\partial^2 L_j}{\partial t^2} \right]_{t_*} \right] d^3 \mathbf{y}. \end{aligned} \quad (14)$$

The equations (10), (12), and (13) are discretized via the boundary element method. Some details are given in the following Section.

4 Numerical examples

4.1 Computational details

Computations have been carried out for data corresponding to an experimental rig with nozzle and end plate hole diameter $d_0 = 2r_0 = 50$ mm [18]. The outer diameter of the end plate is 250 mm. The gap length $\ell = 50$ mm, e.g., equal to d_0 . The mean velocity u_0 of the air-jet is 10 m/s. In the experiments, this value gave the most powerful and stable hole-tone. At 20 °C it corresponds to a Reynolds number $Re = u_0 d_0/\nu \approx 3.3 \times 10^4$ and a Mach number $M = u_0/c_0 \approx 0.03$, where the speed of sound $c_0 = 340$ m/s and the kinematic viscosity $\nu = 1.5 \times 10^{-5}$ m²/s.

The initial vortex core radii are set to $\sigma_j = 0.155r_0$; the choice of this value is simply based on numerical experimentation. In the decay law (7), $a^2 Re = \frac{1}{3}$.

The time step $\Delta t = \frac{1}{80} \frac{d_0}{u_0}$. If vortex roll-up is ignored for the moment, this corresponds to discretization of the shear layer between nozzle exit and end plate into 143 equidistant vortex rings, based on the vortex convection velocity $u_c \approx 0.56u_0$ [18]. With a gap length $\ell = 50$ mm, the distance between the vortex centers is approximately 0.35 mm. As the core thickness is $2\delta_j = 0.155d_0 \approx 7.75$ mm, there is a significant overlap between the vortex rings, as there should be for the discrete vortex method to be sufficiently accurate.

Simulations were typically run for 3400 timesteps; of these the last $2^{11} = 2048$ steps were analyzed by fast Fourier transform, while the first 1352 steps were discarded, as transients. The Nyquist criterion gives the maximum correct frequency as $f_{\text{max}} = 1/2\Delta t = 40u_0/d_0$. With $u_0 = 10$ m/s and $d_0 = 50$ mm, $f_{\text{max}} = 8$ kHz, which is far beyond the range of interest.

The flow-generating upstream nozzle end is represented by 17 vortex panels in radial direction and 18 panels in circumferential direction. The nozzle surface is represented by 17 panels in

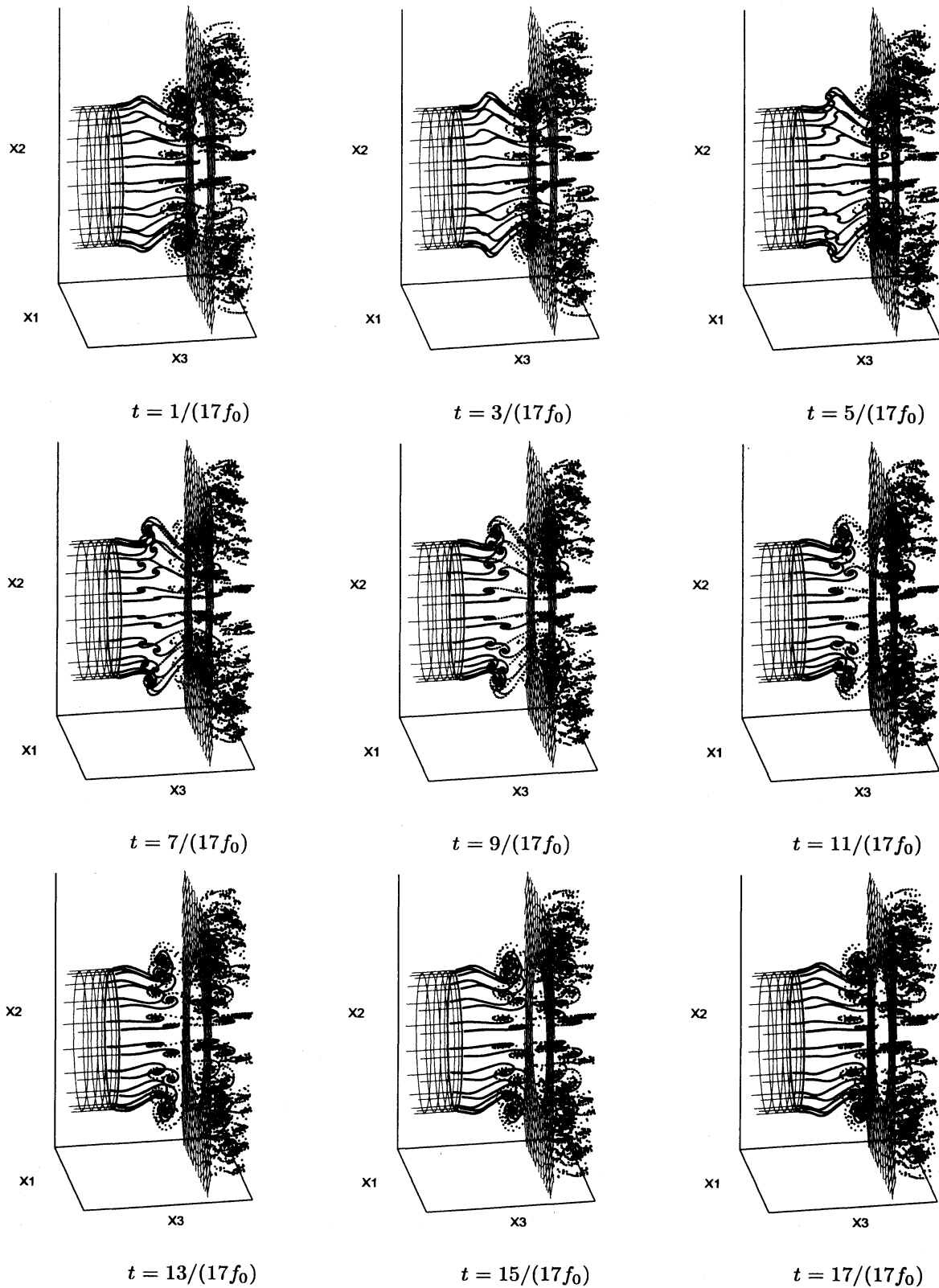


Figure 3: Side view of the jet during one period of oscillation, based on the fundamental hole-tone frequency f_0 [Only the control points of the vortex rings are drawn; not the full rings].

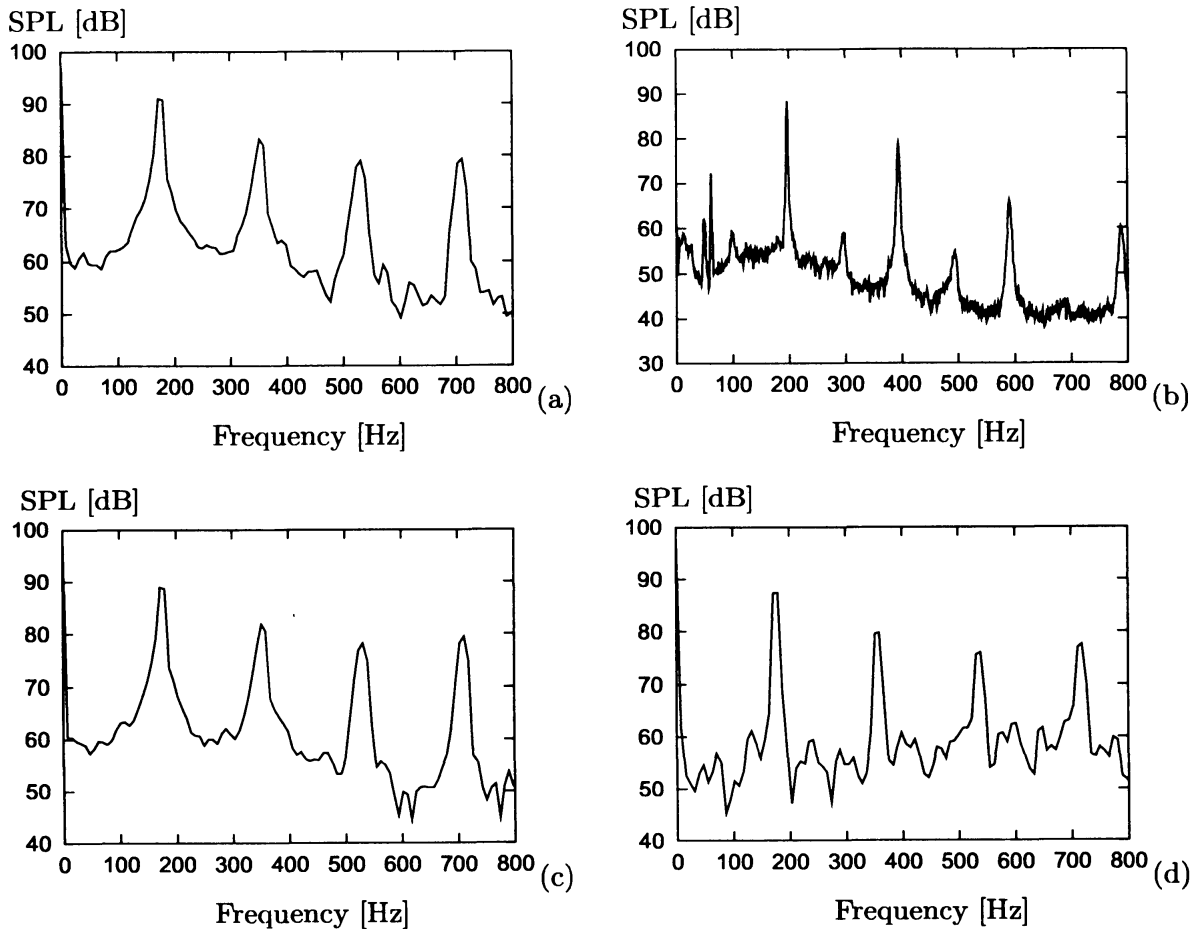


Figure 4: Comparison between computed and experimental frequency spectra for the acoustic pressure fluctuations midway between nozzle exit and end plate, and a distance $1.84d_0$ from the jet axis. [SPL = sound pressure level (in dB); reference 2×10^{-5} Pa]. (a) Computational spectrum. (b) Experimental spectrum. (c) Influence of doubling the number of panels in circumferential direction on the end plate. (d) Influence of decreasing the initial vortex radius from $\sigma_j = 0.155r_0$ to $0.125r_0$.

axial direction and 18 panels in circumferential direction. Finally, the end plate is represented by 23 panels in radial direction and 36 panels in circumferential direction. The panels on the upstream nozzle end and the end plate are uniformly distributed, while the panels on the nozzle surface are concentrated in axial direction towards the nozzle exit.

For the acoustic analysis, the boundary element discretization of the end plate uses the same grid points as the vortex panels. Wells and Renaut [28] recommend that the element lengths (distance between the nodes) should be less than the speed of sound c_0 times the time step Δt , and this criterion is satisfied, although the panels on the outer edge are ‘just on the limit’. Finally, it should be mentioned that, in the computational examples to follow, the retarded time corrections r/c_0 are always very small, and will be neglected.

4.2 Unperturbed flows

4.2.1 Comparison with experiment

A number of side view ‘snapshots’ of the jet during one period of the oscillations are shown in Fig. 3. The computed fundamental frequency $f_0 \approx 175$ Hz; this is about 10 % too low,

compared to the experimentally observed value of 196 Hz.

Fig. 4(a) shows the spectrum (in dB, based on the reference pressure $p_0 = 2 \times 10^5$ Pa) for the acoustic pressure fluctuations, recorded midway between nozzle exit and end plate, and at a distance $r = 1.84d_0$ away from the jet axis. This observation point corresponds to the one used in the experiments of Nakano et al. [18]. Data were recorded at this point only; accordingly, any sound pressure data in the present paper is for this observation point. Part (b) shows the experimentally obtained spectrum. As just mentioned above, the theoretical value of the fundamental component $f_0 \approx 175$ Hz while the experimental value is 196 Hz. Unfortunately the discrepancy is amplified in the higher harmonics $2f_0, 3f_0, \dots$, in the sense that the absolute error becomes larger and larger. The subharmonics at $\frac{1}{4}f_0, \frac{1}{2}f_0, \frac{3}{2}f_0, \dots$, are not represented well either in the computational model. It is shown in [15] that acoustic feedback velocities are able to amplify these subharmonics, particularly $\frac{1}{4}f_0$.

The influence of doubling the number of panels in circumferential direction (to 72 panels) is illustrated by Fig. 4(c). The peak of the fundamental component f_0 may be slightly lower than in Part (a) but otherwise, no significant changes are seen.

In Fig. 4(d) the initial thickness of the free vortex rings is decreased from $\sigma_j = 0.155r_0$ to $0.125r_0$. [The number of panels on the end plate in circumferential direction is again 36.] Comparing again with Part(a) it is seen that the components at $f_0, 2f_0, 3f_0, \dots$, are more 'distinct', but the peak levels and numerical values (of the frequencies) are virtually unchanged.

4.3 Flows subjected to non-axisymmetric perturbations

4.3.1 The nozzle waves/vibrations

This section will be concerned with the effect of shape perturbations applied to the mouth of the nozzle. Two types of perturbations will be considered: shell (or edge) vibrations in the form of (i) standing waves and (ii) travelling (rotating) waves. To describe these perturbations, let the y_3 axis (of the (y_1, y_2, y_3) coordinate system) coincide with the symmetry axis of the jet, as indicated in Fig. 5.

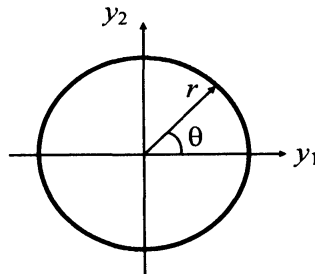


Figure 5: Polar coordinate system used to describe the nozzle shape perturbations.

In case of a standing wave perturbation, the shape of the nozzle edge is given by

$$\mathbf{y}(r, \theta, t) = \mathbf{y}_0(r, \theta) + \mathbf{y}_\epsilon(\epsilon, \theta) \cos(\Omega_s t + \psi), \quad (15)$$

where the first term

$$\mathbf{y}_0(r, \theta) = (r \cos \theta, r \sin \theta, y_3)^T \quad (16)$$

describes the undisturbed nozzle edge; the second term

$$\mathbf{y}_\epsilon(\epsilon, \theta) = \epsilon \sin(n_p \theta) (\cos \theta, \sin \theta, 0)^T \quad (17)$$

describes the static edge deformation; finally, Ω_s is the cyclic frequency of the standing wave and ψ is a phase angle (to be able to impose a phase difference, relative to the flow).

In case of a travelling (rotating) wave perturbation, the shape of the nozzle edge is given by

$$\mathbf{y}(r, \theta, t) = \mathbf{y}_0(r, \theta) + \mathbf{R}(t)\mathbf{y}_\epsilon(\epsilon, \theta), \quad (18)$$

where the matrix

$$\mathbf{R}(t) = \begin{pmatrix} \cos(\Omega_r t + \psi) & -\sin(\Omega_r t + \psi) & 0 \\ \sin(\Omega_r t + \psi) & \cos(\Omega_r t + \psi) & 0 \\ 0 & 0 & 1 \end{pmatrix} \quad (19)$$

imposes a rotation with angular frequency Ω_r and phase angle ψ .

In the y_3 direction the amplitude decreases linearly, from ϵ at the nozzle edge to zero at a distance r_0 upstream from the edge.

Edge vibration modes 2 through 5 are shown in Fig. 6.

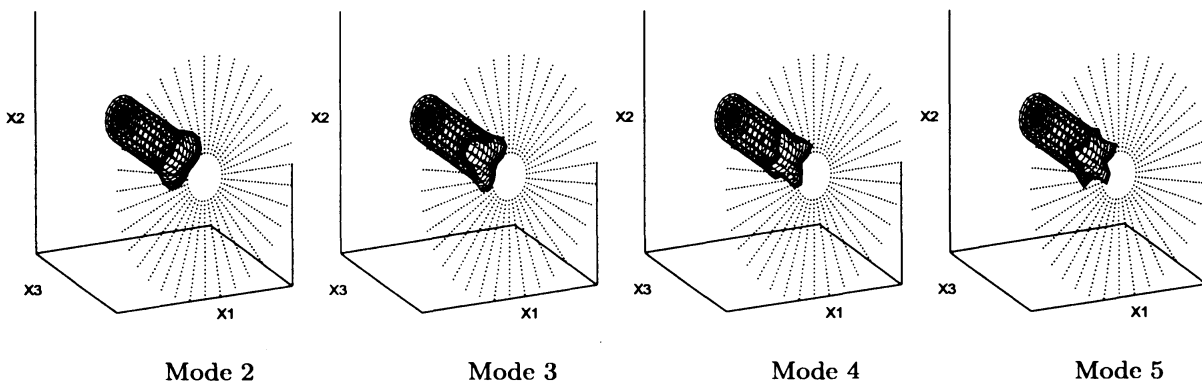


Figure 6: Illustration of the perturbation mechanism (actuator model). [For purpose of illustration the amplitude is exaggerated. Also, the end plate is represented just by its nodal points.]

4.3.2 Standing wave perturbation

The first numerical example will consider a standing wave perturbation. The parameters are chosen as follows: mode number $n_p = 3$, perturbation frequency $f_s = \Omega_s/2\pi = \frac{200}{3}$ Hz, and perturbation amplitude $\epsilon = \frac{1}{15}r_0$. The phase angle $\psi = 0$.

The effect of this perturbation on the appearance of the flow is illustrated in Fig. 7. [It is noted that the nozzle grid data were not saved with the flow ‘snapshots’. It may thus appear as if the vortices are separated above or below the nozzle edge at some control points.]

Comparison of Fig. 7 with Fig. 3 indicates that the coherence of the ‘smoke rings’ is partially destroyed by the perturbations. The effect of these (perturbations) on the sound pressure spectrum (again for an observation point located midway between nozzle exit and end plate and a distance $1.84d_0$ from the jet axis) is shown in Fig. 8(a), which should be compared with Fig. 4(a). In addition to the reduction of the peak value of the fundamental frequency component f_0 , it is seen that the higher harmonics $2f_0, 3f_0, \dots$, virtually are eliminated. At the same time the level of the ‘broad band noise’ has been increased significantly.

Fig. 8 (b) is for the case with mode number $n_p = 5$, and otherwise the same parameters. Comparing again with with Fig. 4(a) it is seen that the amplitude reduction is much more modest this time; a couple of dB’s, at most. Furthermore, a significant amount of broadband noise has been generated.

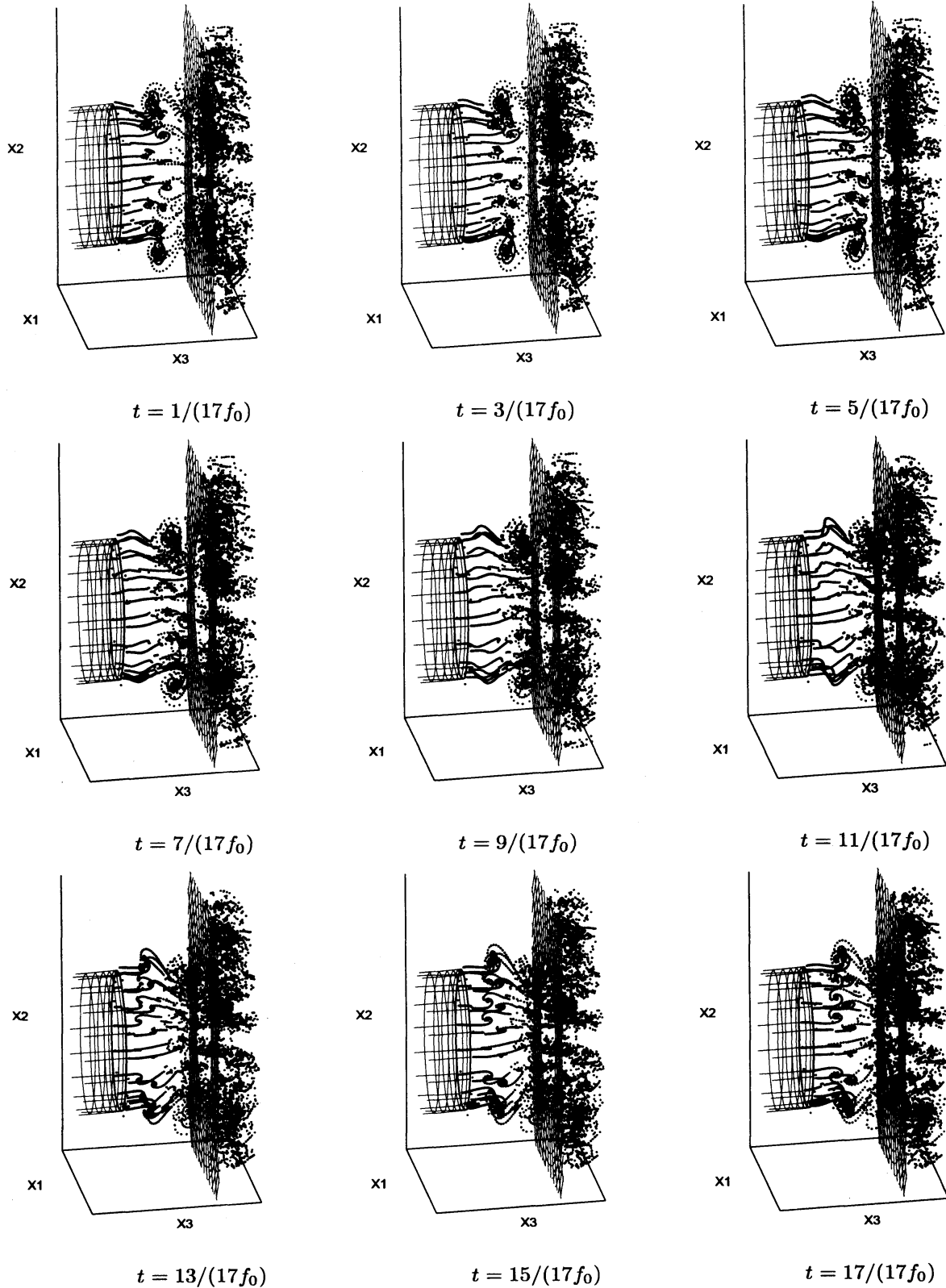


Figure 7: The jet subjected to a standing wave perturbation in mode $n_p = 3$ (as shown in Fig. 6). Side view during one period of oscillation, based on the fundamental hole-tone frequency f_0 of the unperturbed problem.

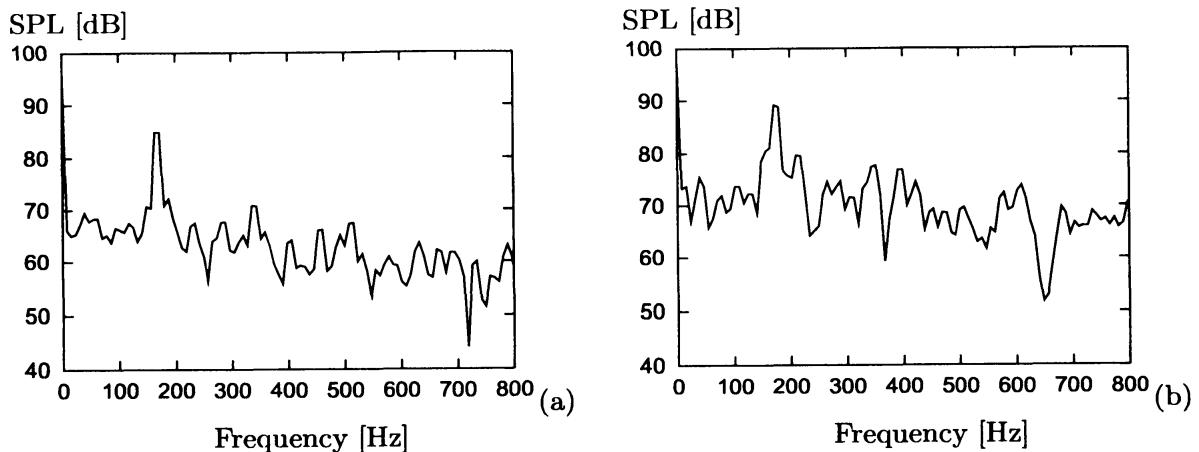


Figure 8: Spectrum of the acoustic pressure fluctuations with a standing wave perturbation. (a) Mode $n_p = 3$. (b) Mode $n_p = 5$.

4.3.3 Travelling (rotating) wave perturbation

The last two examples will be concerned with rotating perturbations. Here, the mode number $n_p = 3$, and the rotational frequency $f_r = \Omega_r/2\pi = \frac{200}{3}$ Hz. Again, the phase angle $\psi = 0$.

In the first example the perturbation amplitude $\epsilon = \frac{1}{150}r_0$ (i.e., $\frac{1}{10}$ of the amplitude in the earlier examples). The influence of this perturbation on the flow field is illustrated by Fig. 9.

It is seen that a swirling jet is generated. While the shear layer still rolls up into ‘smoke rings’, these are less coherent than by the unperturbed flow. Accordingly, they impact the end plate in a much more ‘soft’ manner, and the generation of a distinct tone (at f_0) is replaced largely by broad-band noise, as illustrated by Fig. 10 (a). Part (b) is for a case with perturbation amplitude $\epsilon = \frac{1}{15}r_0$, as in the examples with standing waves. Comparing with Fig. 4(a), it is seen that the sound generation has been reduced by approximately 20 dB.

4.3.4 Summary of the effect of standing and travelling wave perturbations

The geometrical effects of the considered flow perturbations are summarized in Fig. 11, which shows the vortex ring nodal points located between the end plate and a distance $\frac{1}{20}d_0$ upstream from it, at instants where ‘smoke rings’ are about to impact. The full circle represents the hole in the end plate.

Part (a) is for the unperturbed flow. There is perfect axisymmetry, and the vortex rings impacts on the end plate with their full circumference.

Part (b) is for the case with a standing wave perturbation in mode $n_p = 3$ and with amplitude $\epsilon = \frac{1}{15}r_0$. The smoke rings still appear to be coherent. [Refer again to Fig. 7.] It is noted also that the variations in axial velocity between the nodal points of each vortex ring are small. The shape distortion implies however that only a limited part of the circumference impacts ‘head-on’ onto the end plate. This appears to be main sound-limiting mechanism.

Part (c) is for the standing wave perturbation in mode $n_p = 5$ (and otherwise same parameter values). It appears that the coherence of the ‘smoke rings’ are not that different from the previous case with $n_p = 3$. The wave of higher mode number is however not so efficient in hindering portions of the smoke ring from impacting the plate; hence the sound reduction is lower than by perturbations in mode 3.

Part (d) is for the rotating wave perturbation in mode $n_p = 3$ and with amplitude $\epsilon = \frac{1}{150}r_0$. The (apparently) random locations of the vortex nodal points indicate that the smoke rings have less coherence than in any of the previous cases (a), (b), and (c), and accordingly, produce less

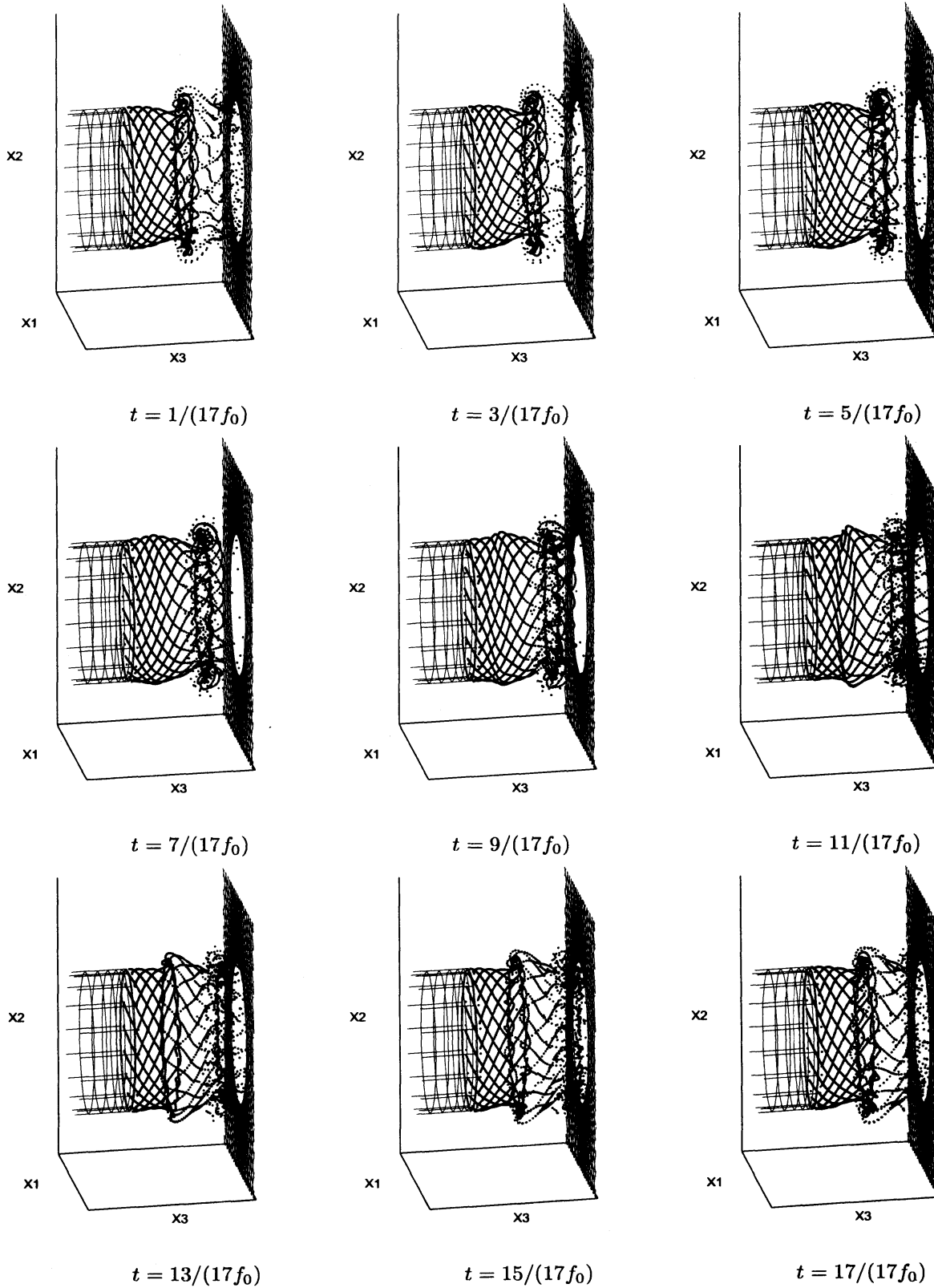


Figure 9: Appearance of the jet subjected to a rotating perturbation in mode $n_p = 3$ (as shown in Fig. 6) and with amplitude $\epsilon = \frac{1}{150}r_0$. [f_0 is the fundamental hole-tone frequency of the unperturbed problem.]

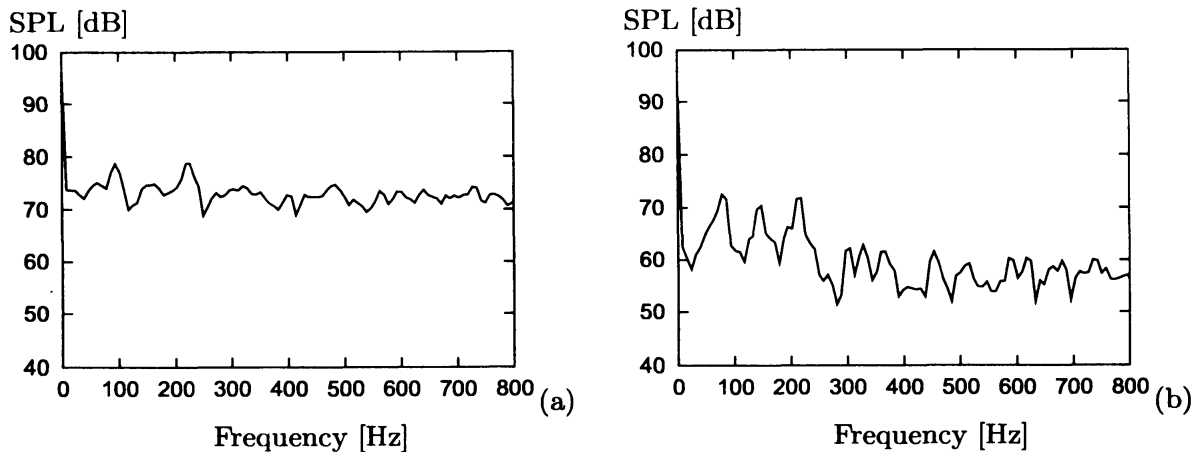


Figure 10: Spectrum of the acoustic pressure fluctuations with a rotating wave perturbation in mode $n_p = 3$. (a) Amplitude $\epsilon = \frac{1}{150}r_0$. (b) Amplitude $\epsilon = \frac{1}{15}r_0$.

sound. In part (e) the amplitude $\epsilon = \frac{1}{15}r_0$, as by the standing wave examples. This results in an even more scattered distribution of the vortex ring nodal points, and further reduction of the sound pressure.

The reason for the scattering of the control point placements may be found in the fact that the convection velocity of a vortex ring is proportional to its curvature [2]. When the shape of a vortex ring is perturbed, sections with larger curvature (than the mean value, say) will move faster than sections with smaller curvature. By the rotating perturbations, the curvature of the vortex rings to be released from the nozzle is continuously changing, seen from the control points along the circumference of the nozzle. Thus, the convection velocity of consecutive (neighboring) control points are always different. Hence, their positions are ‘randomized’.

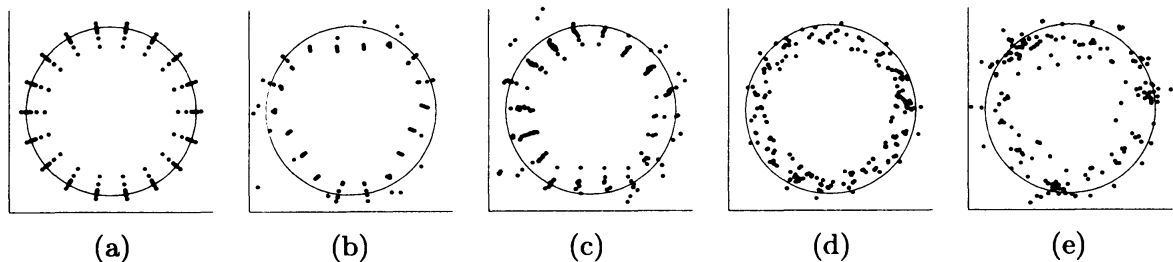


Figure 11: Cross sectional view of the jet. Shown are the vortex ring nodal points located between the end plate and a distance $\frac{1}{20}d_0$ upstream from it. The full circle represents the hole in the end plate. (a) Unperturbed flow. (b) Standing wave perturbation, $n_p = 3$, $\epsilon = \frac{1}{15}r_0$. (c) Standing wave perturbation, $n_p = 5$, $\epsilon = \frac{1}{15}r_0$. (d) Rotating wave perturbation, $n_p = 3$, $\epsilon = \frac{1}{150}r_0$. (e) Rotating wave perturbation, $n_p = 3$, $\epsilon = \frac{1}{15}r_0$.

5 Concluding remarks

The effects of non-axisymmetric perturbations of the nozzle mouth on the sound generation in the hole-tone feedback problem has been investigated. Only a few examples have been given in the present paper; a thorough parameter study will be the subject of subsequent work. The determination of the optimum perturbation frequency, mode number, and phase relation (between flow and nozzle oscillations) will be an interesting problem for future research. It is

also a difficult problem, when posed as an optimization problem, since the mode numbers are integers.

Acknowledgement

The support of the present project through a JSPS Grant-in-Aid for Scientific Research (No. 18560152) is gratefully acknowledged.

References

- [1] W. T. Ashurst and E. Meiburg, Three-dimensional shear layers via vortex dynamics, *J. Fluid Mech.* 189 (1988) 87-116.
- [2] G. K. Batchelor, *An Introduction to Fluid Dynamics*, Cambridge University Press, Cambridge, 1967.
- [3] R. C. Chanaud and A. Powell, Some experiments concerning the hole and ring tone, *J. Acoust. Soc. Am.* 37 (1965) 902-911.
- [4] G.-H. Cottet and P. D. Koumoutsakos, *Vortex Methods: Theory and Practice*, Cambridge University Press, Cambridge, 2000.
- [5] Y. Fukumoto and F. Kaplanski, Global time evolution of an axisymmetric vortex ring at low Reynolds numbers, *Phys. Fluids* 20 (2008) 053103.
- [6] P. Holmes, J. L. Lumley, and G. Berkooz, *Turbulence, Coherent Structures, Dynamical Systems and Symmetry*, Cambridge University Press, Cambridge, 1996.
- [7] M. S. Howe, Contributions to the theory of aerodynamic sound, with applications to excess jet noise and the theory of the flute, *J. Fluid Mech.* 71 (1975) 625-673.
- [8] M. S. Howe, *Acoustics of Fluid-Structure Interactions*, Cambridge University Press, Cambridge, 1998.
- [9] M. S. Howe, *Theory of Vortex Sound*, Cambridge University Press, Cambridge, 2003.
- [10] T. Kambe and T. Minota, Acoustic wave radiated by head-on collision of two vortex rings, *Proc. R. Soc. Lond. A* 386 (1983) 277-308.
- [11] N. Kasagi, Toward smart control of turbulent jet mixing and combustion, *JSME Int. J. Ser. B* 49 (2006) 941-950.
- [12] J. Katz and A. Plotkin, *Low-Speed Aerodynamics*, Cambridge University Press, Cambridge, 2001.
- [13] Y. Kawai and T. Terai, A numerical method for the calculation of transient acoustic scattering from thin rigid plates, *J. Sound Vib.* 141 (1990) 83-96.
- [14] M. A. Langthjem and M. Nakano, A numerical simulation of the hole-tone feedback cycle based on an axisymmetric discrete vortex method and Curle's equation, *J. Sound Vib.* 288 (2005) 133-176.
- [15] M. A. Langthjem and M. Nakano, Numerical study of the hole-tone feedback cycle based on an axisymmetric formulation, *Fluid Dyn. Res.* (2010) in press.

- [16] A. Leonard, Computing three-dimensional incompressible flows with vortex elements, *Annu. Rev. Fluid Mech.* 17 (1985) 523-559.
- [17] D. Meganathan and E. Vakili, An experimental study of acoustic and flow characteristics of hole tones. In: 44th AIAA Aerospace Sciences Meeting and Exhibit, 9-12 January 2006, Reno, Nev. AIAA 2006-1015, 2006, 14 pp.
- [18] M. Nakano, D. Tsuchidoi, K. Kohiyama, A. Rinoshika, and K. Shirono, Wavelet analysis on behavior of hole-tone self-sustained oscillation of impinging circular air jet subjected to acoustic excitation, (In Japanese) *J. Visualization Soc. Japan* 24 (2004) 87-90.
- [19] E. Naudascher and D. Rockwell, *Flow-Induced Vibrations*, Dover Publications, New York, 2005.
- [20] A. Pikovsky, M. Rosenblum, and J. Kurths, *Synchronization: A Universal Concept in Nonlinear Sciences*, Cambridge University Press, Cambridge, 2001.
- [21] A. Powell, Theory of vortex sound, *J. Acoust. Soc. Am.* 36 (1964) 177-195.
- [22] Lord Rayleigh, *The Theory of Sound*, Vol. II, Dover Publications, New York, 1945.
- [23] E. Rivoalen and S. Huberson, Numerical simulation of axisymmetric viscous flows by means of particle method, *J. Comput. Phys.* 152 (1999) 1-31.
- [24] D. Rockwell and E. Naudascher, Self-sustained oscillations of impinging free shear layers, *Annu. Rev. Fluid Mech.* 11 (1979) 67-94.
- [25] D. Rockwell, Oscillations of impinging shear layers, *AIAA J.* 21 (1983) 645-664.
- [26] P. G. Saffman, *Vortex Dynamics*, Cambridge University Press, Cambridge, 1992.
- [27] T. Terai, On calculation of sound fields around three dimensional objects by integral equation methods, *J. Sound Vib.* 37 (1980) 71-100.
- [28] V. L. Wells and R. A. Renaut, Computing aerodynamically generated noise, *Annu. Rev. Fluid Mech.* 29 (1997) 161-199.